Supporting Information

Accelerated Synthesis of Framework Titanium-Substituted Beta Zeolite Using N-methyl-2-pyrrolidone and Beta seeds

Hedieh Tabatabaeizadeh [a], Francesca Rosso [a], Francesca Bonino [a], Silvia Bordiga [a], Valentina Crocellà [a], Miguel A. Camblor [b], Matteo Signorile [a]

[a] *Department of Chemistry, NIS Centre, INSTM Research Unit, Università di Torino, Via G.Quarello 15/A and Via P. Giuria 7, Turin 10135, Italy.*

[b] *Instituto de Ciencia de Materiales de Madrid, Consejo Superior de Investigaciones Científicas (ICMM-CSIC), c/Sor Juana Inés de la Cruz 3, 28049, Madrid, Spain.*

X-ray Diffraction Patterns

Figure S1a shows the XRD pattern of Beta-N-24h sample during different treatments. A noticeable shift of the main diffraction peak around 22.5° toward higher 2θ values is observed after dealumination.[1] This shift indicates a slight contraction of the unit cell, which can be attributed to the replacement of longer Al–O bonds (~1.75 Å) with shorter Si–O bonds (~1.61 Å) upon removal of framework aluminium.[1,2] Such contraction is a well-known structural consequence of increasing the Si/Al ratio in zeolites, as the framework becomes denser and more siliceous.[10–12] In the present case, the shift observed for Beta-N-24h thus confirms the successful removal of Al species, leading to a more compact and structurally ordered siliceous network. This enhancement can also arise from the elimination of a thin amorphous layer deposited on the crystal surface, which reduce diffuse scattering and yield cleaner diffraction profiles, as previously discussed by Yoshioka *et al.*[12]

Additionally, to assess the influence of the sequence of N-methyl-2-pyrrolidone (NMP) addition on the crystallization pathway, several syntheses were performed by introducing NMP at different stages of gel preparation. When NMP was added prior to or after the titanium precursor (TEOT), the resulting materials exhibited well-defined diffraction patterns consistent with the Beta topology, confirming the formation of a highly crystalline Ti-Beta phase (Figure S1). These samples displayed the characteristic reflections at 2θ ≈ 7.6°, 21.5°, 22.5°, 25.3°, 27.0° and 29.6° with no detectable secondary phases such as anatase or amorphous residues. In contrast, when NMP was introduced later in the synthesis sequence, for instance before the addition of HF, as in the Ti-Beta-N-F-72h-3 sample, the final product was amorphous, lacking the characteristic Beta reflections. This may indicate that the late introduction of NMP limits its ability to promote gel homogenization and uniform distribution of silicon and titanium species. When NMP is present from the earliest stages, it enhances the dispersion and solvation

of silica and titanium precursors, creating a more homogeneous reaction medium that facilitates the formation of well-structured nuclei. Conversely, adding NMP after partial gelation reduces its capacity to interact effectively with the developing network, leading to phase separation and the formation of disordered, non-crystalline products (Figure S1b).

Furthermore, the presence of NMP from the beginning also influence the local concentration and distribution of TEA^+ cations, increasing their effectiveness as structure-directing agents. The combination of a homogeneous gel environment and favourable TEA^+-silicate interactions accelerate nucleation and promotes the rapid formation of the Beta framework. Therefore, the timing of NMP addition plays a crucial role in controlling gel uniformity, charge distribution, and ultimately the crystallinity of Ti-Beta zeolite.

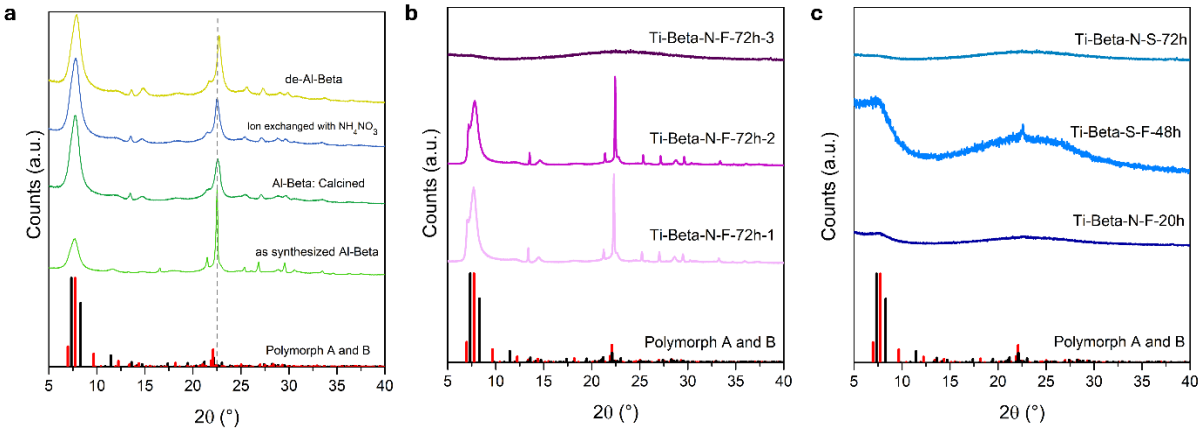

Figure S1. X-ray diffraction patterns of a) Beta-N-24h after different treatments, the dashed line indicates the slightly changes of 22.5° peak due to the dealumination process. b) Ti-Beta-N-F-72h samples synthesized with NMP introduced at different stages of the gel preparation (1: before TEOT, 2: after TEOT, 3: right before HF), and c) exploring the effect of HF, seed and NMP in different syntheses. The diffractograms are normalized to their maximum intensity and vertically shifted for the better visualization. Simulated XRD pattern of Beta zeolite (Polymorph A in red and Polymorph B in black) based on IZA database.

Scanning electron microscopy (SEM) and Energy-dispersive X-ray (EDX) Analysis

SEM analysis indicates that the overall crystal morphology of Beta zeolite is preserved after post-synthetic modification. The parent and dealuminated samples exhibit comparable particle size and shape, suggesting that the ion-exchange and subsequent acid washing treatments do not induce noticeable structural degradation or crystal fragmentation. Energy-dispersive X-ray (EDX) analysis further supports the effectiveness of the dealumination treatment. While the parent Beta sample shows the expected presence of aluminium, the de-Al-Beta exhibits no detectable Al signal within the instrumental detection limits.

Table S1. EDX results of Al-Beta and de-Al-Beta.

Sample	Al/Si molar ratio	Al_2O_3 wt%	Na/Si molar ratio
Al-Beta	0.0914	7.76	0.039
De-Al-Beta	-	-	-

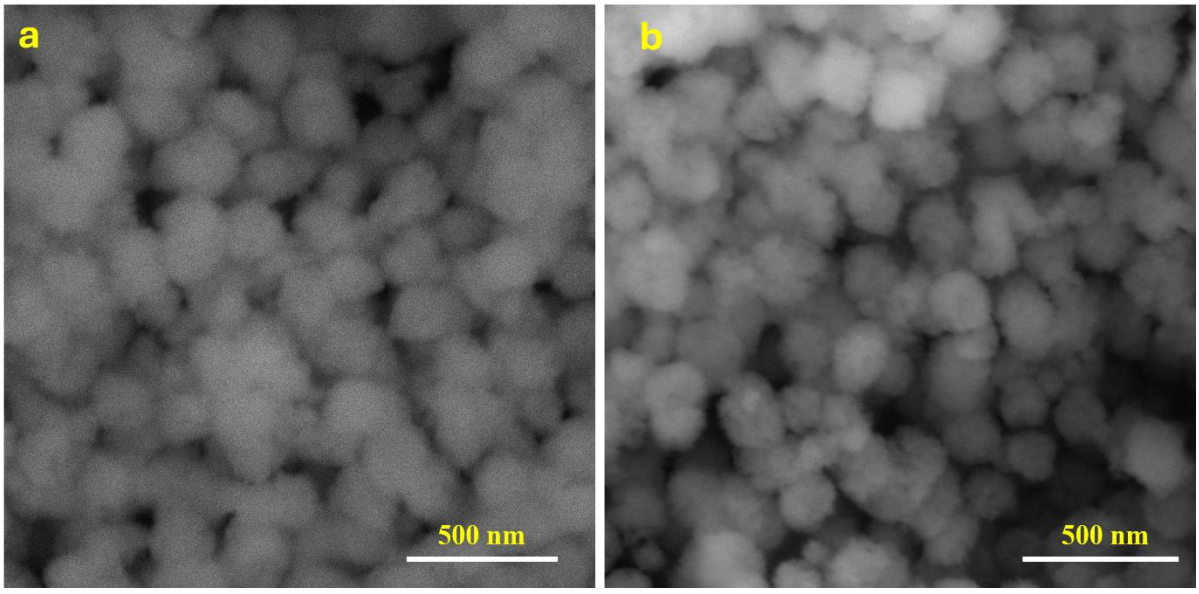

Figure S2. SEM images of a) Al-Beta, 150kx magnification, and (b) de-Al-Beta, 150kx magnification.

SEM images of Beta-N-24h (de-Al-Beta), Ti-Beta-F-336h, Ti-Beta-N-F-72h and Ti-Beta-N-S-F-20h samples are shown in Figure S2. These additional images complement the morphological analysis presented in the main text, highlighting the evolution of crystal size and morphology as a function of synthesis time, and presence of seed and NMP. In particular, samples synthesized with both NMP and seed show smaller, more uniform crystals compared to those synthesized with NMP alone, consistent with faster nucleation and crystal growth. Furthermore, only Beta-N-24h, prepared under OH^- conditions (without HF), exhibits nanosized crystallites.

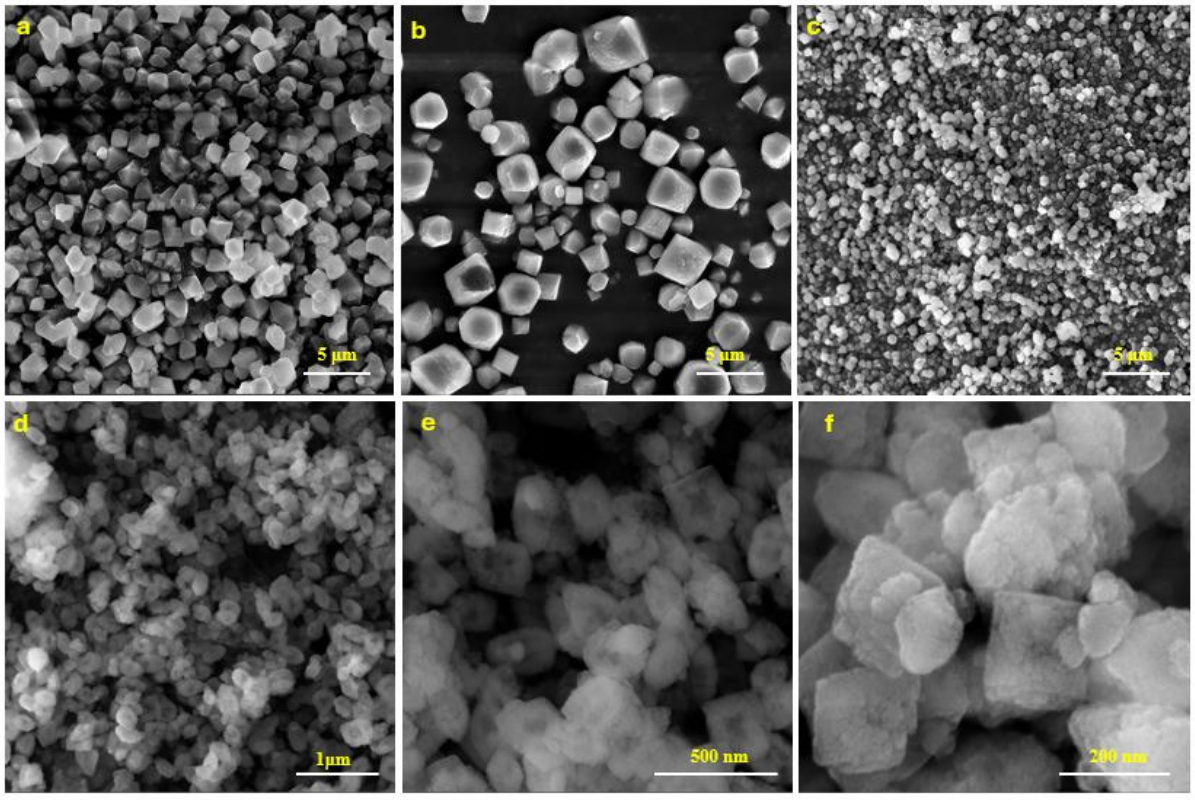

Figure S3. SEM images of (a) Ti-Beta-F-336h, (b) Ti-Beta-N-F-72h, (c) Ti-Beta-N-S-F-20h, and d,e,f) Beta-N-24h. (a-c) 10kx magnification, (d) 60kx magnification, (e) 170kx magnification, (f) 400kx magnification.

BET & Langmuir Linear Fitting Plots

The linear fitting ranges used for BET and Langmuir surface area calculations are reported for each sample to demonstrate the reliability of the selected pressure interval in Figure S3 and 4, respectively. The plots exhibit a clear linear region in the relative pressure (P/P_0) range of approximately 0.008-0.04 (p/p°) for the BET model and 8-18 (kPa) for the Langmuir model.

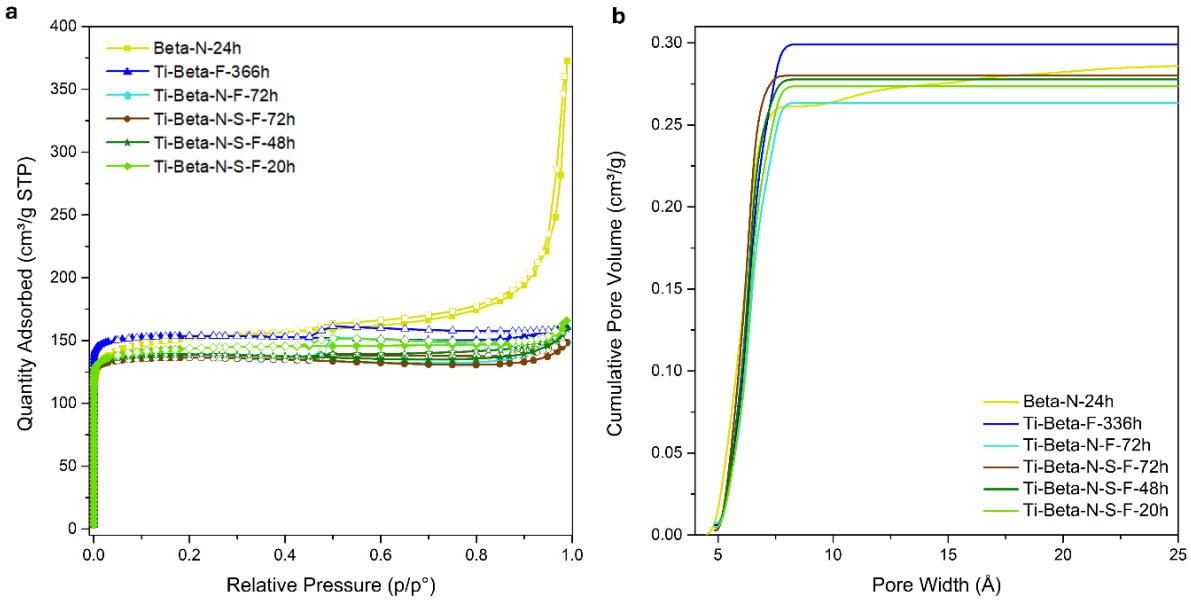

Figure S4. a) N_2 adsorption–desorption isotherms at -196 °C of the Ti-beta samples. , and b) Cumulative pore volume (cm^3/g) vs Pore Width (Å) plot.

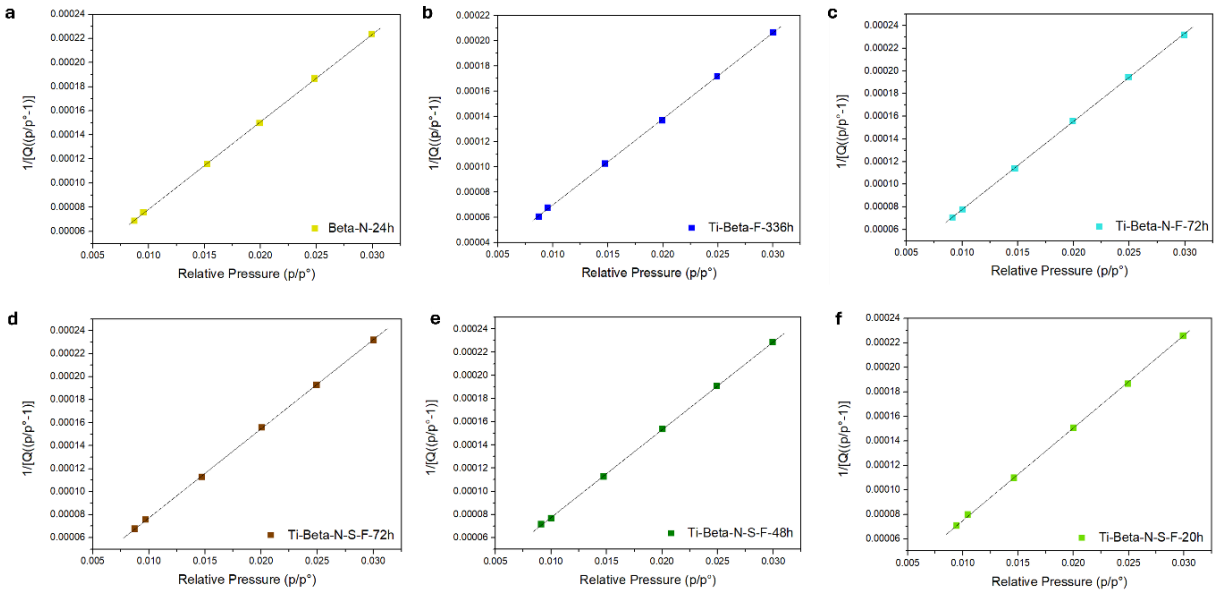

Figure S5. BET linear fitting in the range of 0.008-0.04 (p/p°) for the different samples.

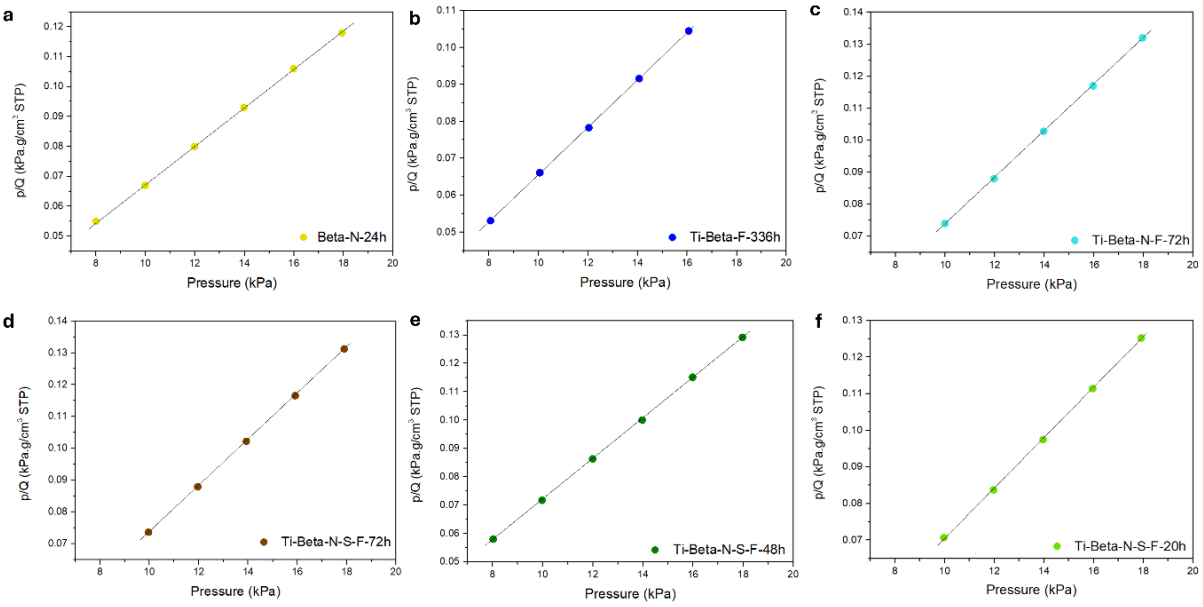

Figure S6. Langmuir linear fitting in the range of 8-18(kPa) for the different samples.

Across the Ti-Beta-N-S-F series (Figure S7), only minor variations are observed in the monolayer capacities derived from both BET and Langmuir models. The BET Q_m decreases from 133 to 129 $cm^3(STP)\ g^{-1}$ (≈3% deviation), while the Langmuir Q_m decreases from 146 to 137 $cm^3(STP)\ g^{-1}$ (≈6% deviation) between 20 and 72 h. These small changes are consistent with the slight reduction in S_{BET} and $S_{Langmuir}$ over time. The slight decrease in S_{BET} from 20 to 72 h originates primarily from a progressive reduction in external surface area ($S_{External}$), while the micropore surface contribution ($S_{Micropore}$) increases. This behaviour is consistent with crystal growth expected at increasing time of hydrothermal treatment: early-stage products may contain a higher fraction of intercrystalline voids, surface roughness, or loosely connected fragments that contribute to external surface area, whereas prolonged crystallization promotes reorganization/densification and smoother particle surfaces, lowering $S_{External}$. In parallel, the increase in $S_{Micropore}$ together with the essentially constant micropore volume (DFT and t-plot) indicates that the intrinsic Beta micropore network is preserved and may become more accessible as crystallization proceeds. This effect is also subtly reflected in the hysteresis region of the N_2 adsorption–desorption isotherms, suggesting minor differences in interparticle voids or crystal packing. Although SEM images show essentially identical crystal morphology and size, slight differences in particle aggregation, packing density, or interconnection between crystals may influence the external surface area accessible to nitrogen. Importantly, the materials remain strictly microporous, as demonstrated by the consistent micropore volumes obtained using two independent methods (DFT and t-plot analyses). Although these approaches rely on different assumptions and therefore yield different absolute values, both techniques consistently show that the micropore volume exhibits only negligible variation across the series ($Vt_{otal} \approx V_{micro}$). This confirms that the intrinsic BEA microporous framework is preserved regardless of synthesis time.

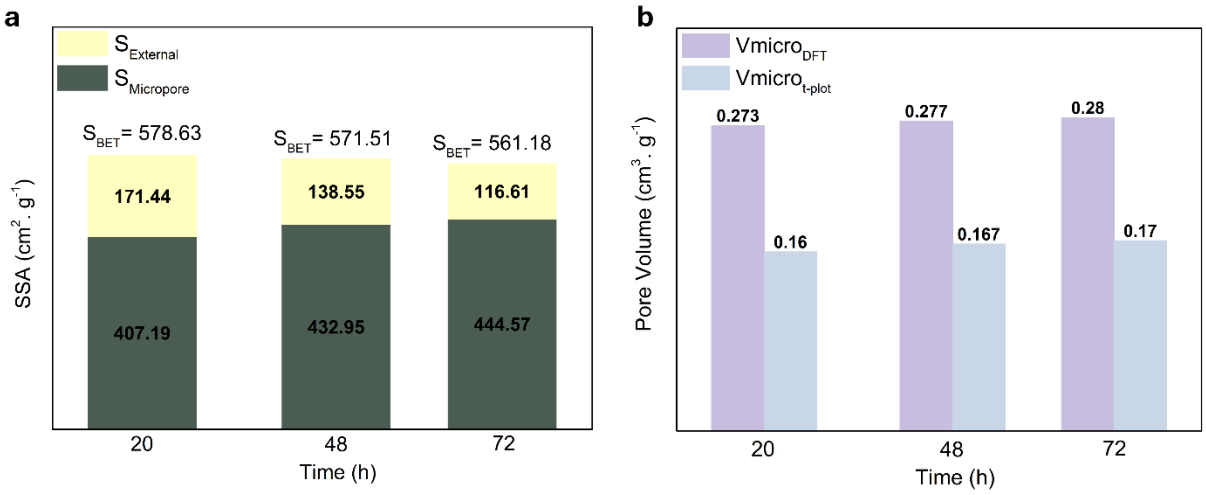

Figure S7. Textural properties of the Ti-Beta-N-S-F series as a function of synthesis time (20–72 h). (a) Specific surface areas (SSA) obtained from BET (SBET), and t-plot external and micropore surface area ($S_{Eexternal}$ and $S_{Micropore}$). (b) Micropore volume determined by DFT and t-plot methods. The statistical thickness range used for the t-plot was 2.4–3.4 Å.

UV-Visible Spectroscopy

The UV–Visible reflectance spectra of the Ti-Beta samples (Figure S6) exhibit the characteristic absorption edge of framework Ti(IV) species in tetrahedral coordination, centred in the 210–230 nm region.[6,8] Upon activation (Figure 4a), all samples show a distinct sharpening and slight blue-shift of this edge compared to their spectra recorded in air (Figure S6). This evolution indicates the removal of adsorbed water and/or organic residues coordinated to the Ti(IV) sites.[5,9] Overall, the spectral evolution before and after activation demonstrates that thermal treatment in vacuum efficiently removes residual organics and water, enhances the optical purity, and reveals the characteristic spectral fingerprint of isolated framework Ti(IV) species, dominant for all samples.

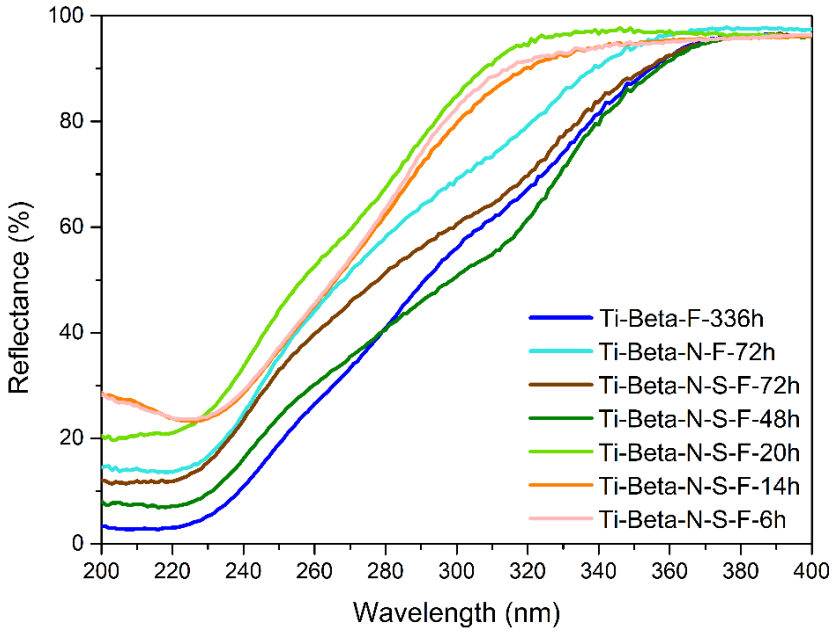

Figure S8. UV–Vis reflectance spectra of Ti-Beta samples in the air.

Raman Spectroscopy

The Raman bands of Al-Beta-N-24h and deAl-Beta-N-24h appear broader compared to the Ti-Beta-N-S-F-20h, which can be attributed to their nanosized crystallites and higher degree of structural disorder. Such broadening arises from phonon confinement effects and increased defect density typical of small crystalline domains.[13] In both deAl-Beta-N-24h, a weak band around 965 cm^{-1} is observed, which is generally assigned to the Si–O stretching vibration perturbed by the presence of framework defects due to the dealumination, reflecting the formation of local silanol nests or vacancies where Al atoms have been removed. Additionally, a distinct band around 700 cm^{-1} is detected for all samples, commonly associated with collective lattice vibrations of the Beta framework.[2,3,7] The relative intensity of this feature is sensitive to defect-induced Si–O stretching; its persistence indicates that, despite structural ordering upon Ti incorporation, some degree of local distortion exists within the Beta lattice.[6,7,11,13,14]

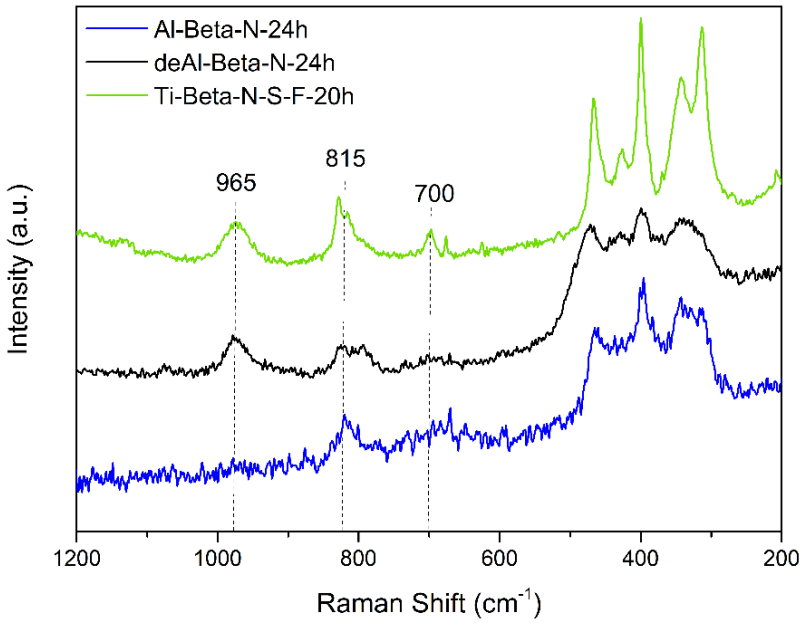

Figure S9. Raman spectra of Al-Beta-N-24h, deAl-Beta-N-24h and Ti-Beta-N-S-F-20h with the 785 nm laser beam. Raman spectra are normalized to their maximum intensity and vertically shifted for visual clarity.

Assessment of Ti Leaching and Framework Integrity after H_2O_2 Treatment

To evaluate the stability of the Ti-Beta-N-S-F-20h upon exposure to H_2O_2, a series of complementary characterizations were carried out to assess possible Ti leaching and framework degradation. XRD was employed to monitor the crystallinity and structural integrity of the zeolite before and after contact with H_2O_2. The preservation of the characteristic reflections of the Beta topology confirmed that no significant framework degradation occurred. EDX analyses of the sample were performed to quantify possible Ti leaching, revealing negligible Ti loss after treatment. SEM images revealed that the morphology and particle size of the crystals remained unchanged after H_2O_2 exposure, indicating the absence of surface erosion or crystal fragmentation. In addition, N_2 physisorption measurements at -196 °C confirmed that the textural properties (surface area and pore volume) were largely maintained, further demonstrating the robustness of the Ti-Beta framework under oxidative conditions. Collectively, these results indicate that the Ti sites in the Beta zeolite are structurally stable and resistant to leaching or crystal destruction upon exposure to hydrogen peroxide.

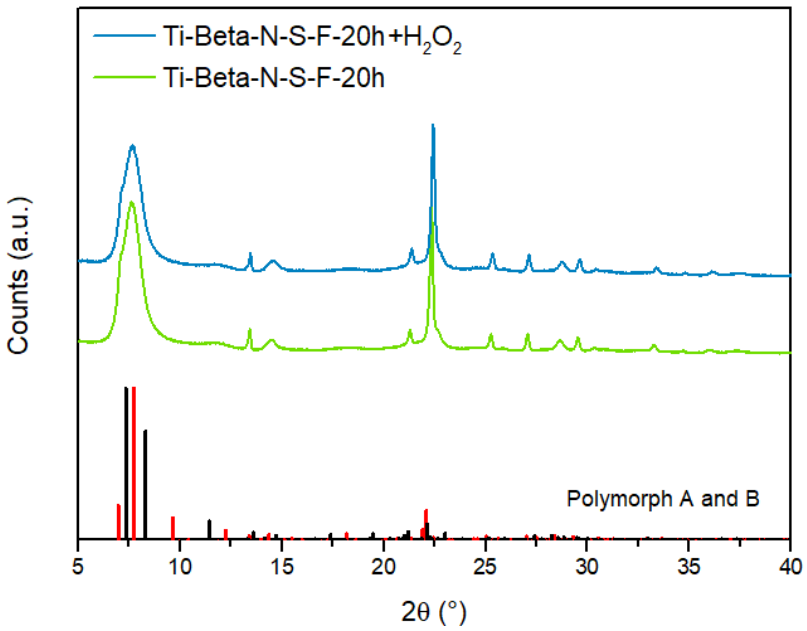

Figure S10. XRD patterns of Ti-Beta-N-S-F-20h before and after the H_2O_2 exposure. The diffractograms are normalized to their maximum intensity and vertically shifted for visual clarity. Simulated XRD pattern of Beta zeolite (Polymorph A in red and Polymorph B in black) based on IZA database.

Table S2. Textural properties of Ti-Beta samples

Sample	Ti/Si molar ratio [a]	TiO_2 wt% [a]	SSA ($m^2\ g^{-1}$)		Pore Volume ($cm^3\ g^{-1}$)		
			S_{BET} [b]	$S_{Langmuir}$ [c]	V_{total}	V_{micro} [d]	V_{meso} [e]
Ti-Beta-N-S-F-20h	0.014	1.89	578.63 ± 0.3	636.19 ± 0.6	0.273	0.273	0
Ti-Beta-N-S-F-20h+H_2O_2	0.014	1.90	566.38 ± 0.24	626.4 ± 1.09	0.279	0.279	0

[a] Determined by EDX measurements, [b] BET range = 0.008-0.040(p/p°), [c] Langmuir range = 8-18(kPa)

[d] Calculated from the cumulative pore volume plot for micropores with size <20 Å, e Vmeso=Vtotal Vmicro.

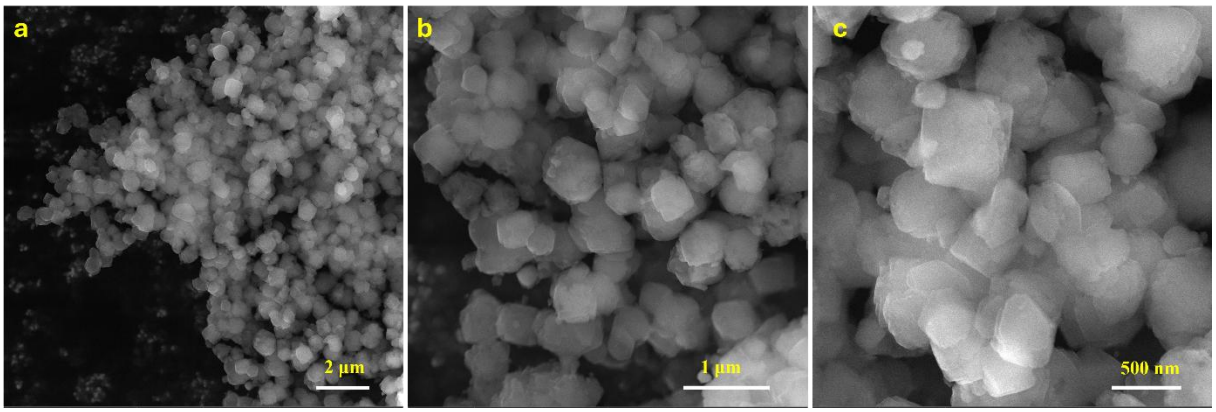

Figure S11. SEM images of Ti-Beta-N-S-F-20h after the H_2O_2 treatment. a) 20kx magnification, (b) 50kx magnification, and (c) 100kx magnification.

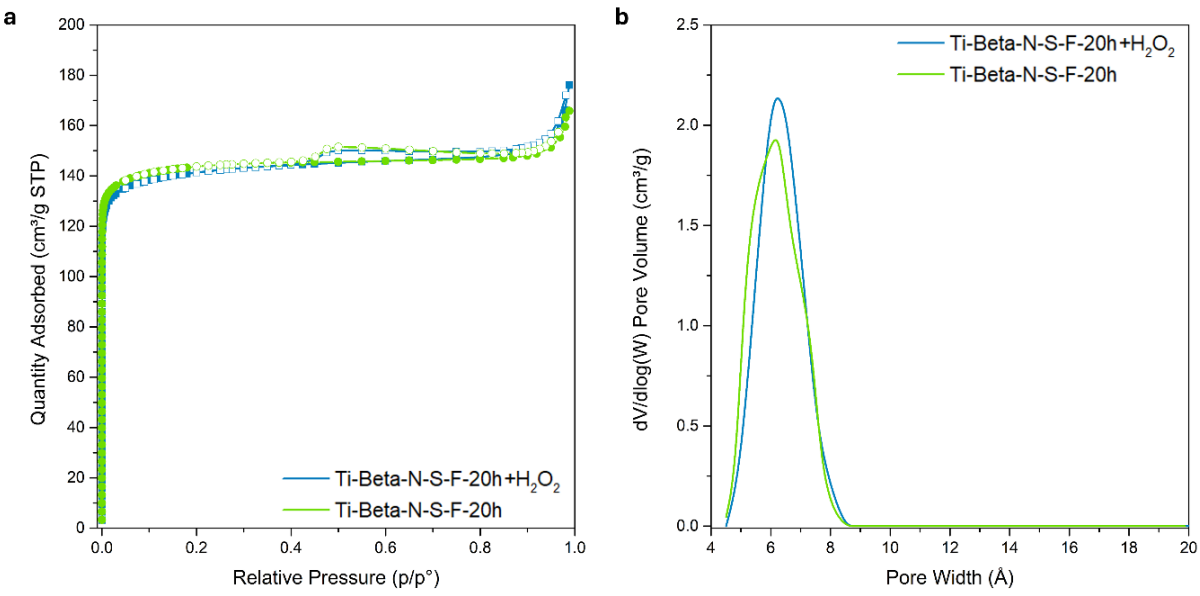

Figure S12. a) N_2 adsorption–desorption isotherms at -196 °C of the Ti-Beta-N-S-F-20h before and after the H_2O_2 exposure, and b) DFT-derived pore size distribution of the same samples.

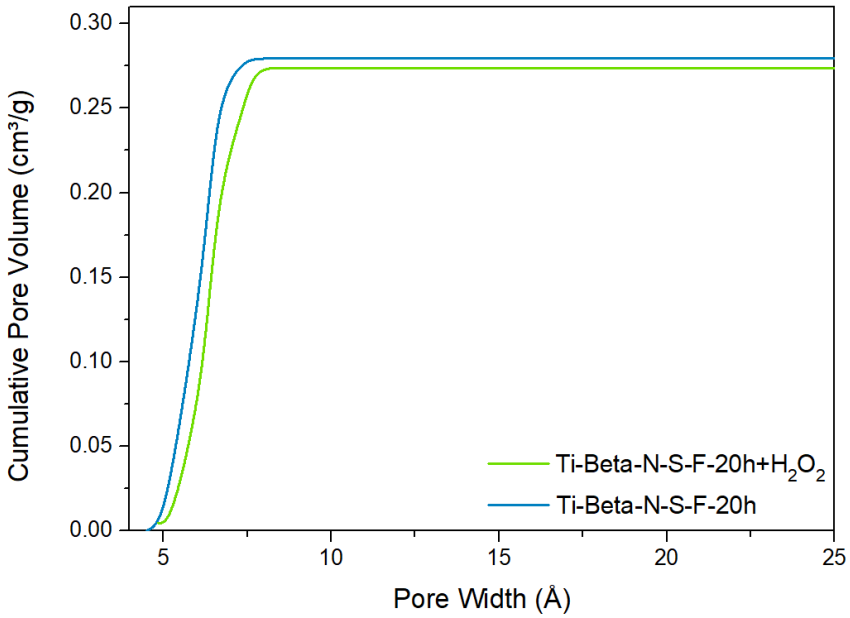

Figure S13. Cumulative pore volume (cm^3/g) vs Pore Width (Å) plot.

Thermogravimetric Analysis and ATR-FTIR Analyses of Uncalcined Samples to Evaluate the Presence of Residual NMP

The TGA curve of the uncalcined Ti-Beta-N-S-F-20h (Figure S14a) exhibits three characteristic regions: (i) desorption of adsorbed water below 150 °C, (ii) decomposition of TEA^+ associated with defect sites between 150–350 °C, and (iii) removal of more strongly confined TEA^+ species above 350 °C. No clear mass drops associated to NMP desorption/decomposition can be identified. As an additional check, moiety sensitive ATR-IR measurements were performed on several as-synthesized (uncalcined) samples (Figure 14b), which show no vibrational features attributable to NMP (e.g., amide C=O at 1650–1670 cm^{-1} or C–N stretching at 1250–1300 cm^{-1} which are highlighted in the spectra below). These results are fully consistent with previous literature reports in which combined solid-state ^{13}C NMR and TGA analyses demonstrated that NMP does not remain occluded in the final zeolite materials and does not act as a structure-directing agent.[4]

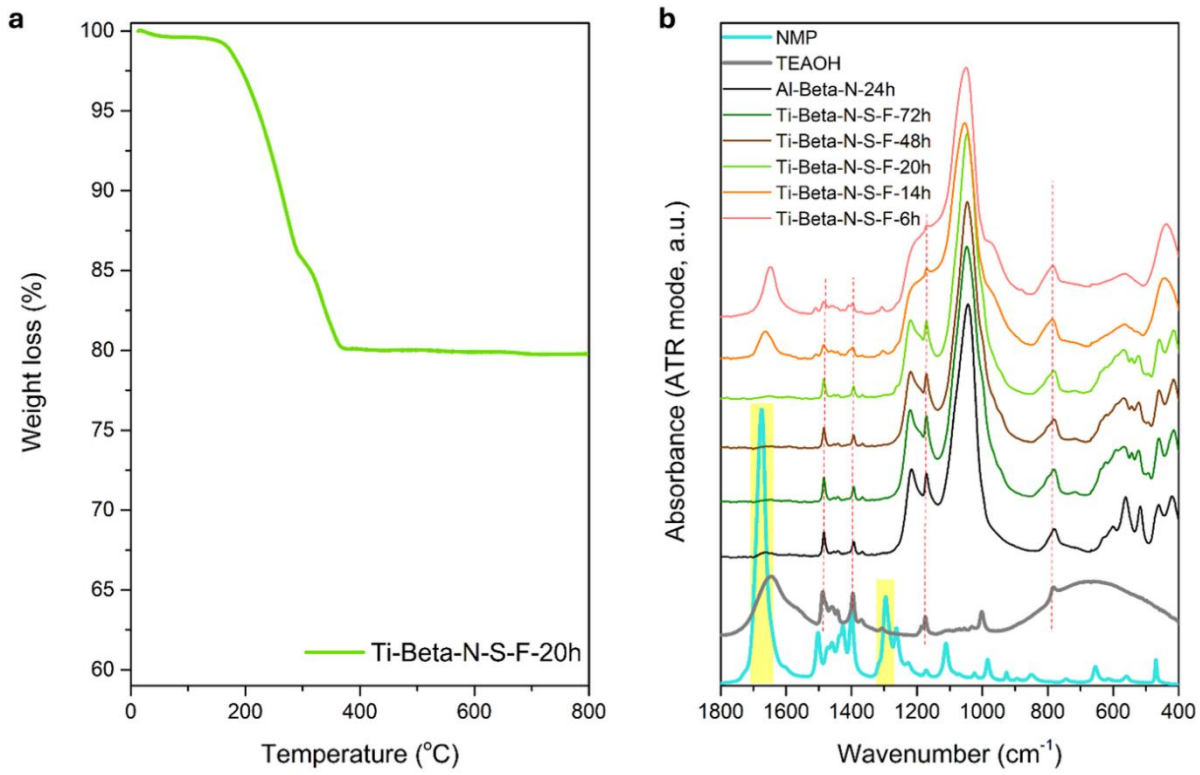

Figure S14. *a) TGA analysis of the uncalcined Ti-Beta-N-S-F-20h. b) ATR-FTIR spectra of uncalcined Ti-Beta-N-S-F series and Al-Beta-N-24h, compared with reference spectra of pure N-methyl-2-pyrrolidone (NMP) and TEAOH.*

References

(1) N. Hoeven, G. Mali, M. Mertens and P. Cool, *Microporous Mesoporous Mater.*, 2019, **288**, 109588.

(2) L. Hong, J. Zang, B. Li, G. Liu, Y. Wang and L. Wu, *Inorganics*, 2023, **11**, 214.

(3) J. M. Newsam, M. M. J. Treacy, W. T. Koetsier and C. B. De Gruyter, in Zeolites: Facts, Figures, Future, ed. H. van Bekkum, E. M. Flanigen and J. C. Jansen, *Elsevier*, Amsterdam, 1989, vol. 49, pp. 467–479.

(4) D. Zhao, W. Chu, Y. Wang, X. Zhu, X. Li, S. Xie, J. An, W. Xin, S. Liu and L. Xu, J. *Mater. Chem. A*, 2018, **6**, 24614–24624.

(5) F. Rosso, A. Rizzetto, A. Airi, K. Khoma, M. Signorile, V. Crocellà, S. Bordiga, S. Galliano, C. Barolo, E. Alladio and F. Bonino, Rationalization of TS-1 Synthesis through the Design of Experiments, *Inorg. Chem. Front.*, 2022, **9**, 3372–3383.

(6) S. Bordiga, C. Lamberti, F. Bonino, A. Travert and F. Thibault-Starzyk, *Chem. Soc. Rev.*, 2015, **44**, 7262–7341.

(7) X. Liang, X. Peng, C. Xia, H. Yuan, K. Zou, K. Huang, M. Lin, B. Zhu, Y. Luo and X. Shu, Ind. Eng. Chem. Res., 2021, 60, 1219–1230.

(8) G. Ricchiardi, A. Damin, S. Bordiga, C. Lamberti, G. Spanò, F. Rivetti and A. Zecchina, J. Am. Chem. Soc., 2001, 123, 11409–11419.

(9) F. Rosso, A. Airi, M. Signorile, E. Dib, S. Bordiga, V. Crocellà, S. Mintova and F. Bonino, Microporous Mesoporous Mater., 2024, 366, 112924.

(10) A. Omegna, M. Vasic, J. A. van Bokhoven, G. Pirngruber and R. Prins, *Phys. Chem. Chem. Phys.*, 2004, **6**, 447–452.

(11) W. J. Roth, B. Gil, K. A. Tarach and K. Góra-Marek, *Chem. Soc. Rev.*, 2025, **54**, 7484 7560.

(12) T. Yoshioka, K. Iyoki, Y. Hotta, Y. Kamimura, H. Yamada, Q. Han, T. Kato, C. A. J. Fisher, Z. Liu, R. Ohnishi, Y. Yanaba, K. Ohara, Y. Sasaki, A. Endo, T. Takewaki, T. Sano, T. Okubo and T. Wakihara, *Sci. Adv.*, 2022, **8**, eabo3093.

(13) H. Richter, Z. P. Wang and L. Ley, *Solid State Commun.*, 1981, **39**, 625–629.

(14) M. A. Camblor, A. Corma and S. Valencia, *Chem. Commun.*, 1996, 2365–2366.